

Observation of ionization-mediated transition from collisionless interpenetration to collisional stagnation during merging of two supersonic plasmas

Auna L. Moser^{a)} and Scott C. Hsu^{b)}

Physics Division, Los Alamos National Laboratory, Los Alamos, New Mexico 87545

(Dated: 3 December 2024)

We present space- and time-resolved experimental data of head-on-merging, supersonic plasma jets (of an argon/impurity mixture) in an initially collisionless regime for counter-streaming ions. The merging begins with collisionless interpenetration followed by a transition to collisional stagnation. The transition occurs due to an experimentally inferred rising mean-ionization level, which rapidly reduces the counter-streaming ion-ion mean free path. The measurements demonstrate a specific mechanism by which a collisionless interaction transitions to a collisional one and constrain collisionality and ionization models for plasmas with complex equation of state.

The dynamics of colliding plasmas plays an important role in, e.g., hohlraum plasmas in inertial confinement fusion,¹ astrophysical shock waves,² and applications such as pulsed laser deposition.³ Colliding plasma interactions can often be in a regime that is neither purely collisional nor purely collisionless, a complicated situation for modeling the interactions.^{4–7} Previous experiments^{8–15} have reported observations of plasma interpenetration on millimeter scales in laser-driven or wire-array Z-pinch experiments. Here we present experimental results from the head-on collision of two larger-scale, railgun-driven supersonic plasma jets in a collisionless regime for counter-streaming ions, in contrast to our recent oblique-jet-merging results that were in a much more collisional regime.^{16,17} In this Letter, we identify collisionless plasma interpenetration transitioning to collisional stagnation between merging supersonic plasmas in an initially collisionless counter-streaming ion regime. Our diagnostic measurements, which span the jet-interaction region, are spatially and temporally well-resolved, allowing us to attribute the transition to an experimentally inferred rising mean ionization \bar{Z} that drastically reduces the inter-jet ion-ion collisional mean free path, which scales as \bar{Z}^{-4} . The data are valuable for validating fundamental physics models of plasma collisionality¹⁸ and ionization, especially in plasmas with complex equations of state (EOS).

Experiments are performed on the Plasma Liner Experiment.^{19–21} Pulsed-power-driven plasma railguns²² launch jets from two directly opposed ports on a spherical vacuum chamber (Fig. 1). Each jet travels ≈ 1.1 m before they interact near chamber center ($z = 0$ cm). The working gas in the experiments presented here is argon. The difference between chamber pressure rise after a plasma shot and after injection of only neutral gas suggests the possibility of significant impurity levels in

the plasma jet.^{16,17} Supported by observations of oxygen and aluminum spectral lines, we can reasonably deduce that impurities come from the railgun insulator material (zirconium-toughened alumina), and so we estimate relative impurity percentages based on their relative abundance in the insulator. An impurity sensitivity analysis comparing bounding cases of 60% impurities, based on the chamber pressure difference, and 10% impurities, chosen due to the appearance of impurity spectral lines at all times of interest, shows that our collisionality-based physics conclusions are independent of the impurity percentage assumed within these bounds (see Table I). We also consider mixtures with small amounts of carbon and hydrogen, with no significant difference in results. The analysis assuming a 40% argon, 60% impurities mixture provides the most conservative collision lengths (i.e., shortest) and so will be used here. At the time of interaction the jets have ion density $n_i \sim 10^{14}$ cm⁻³, electron temperature $T_e \approx 1–3$ eV, and relative velocity $v_{rel} \approx 90$ km/s, with radius ≈ 15 cm and length ≈ 50 cm. We expect the magnetic field to be ~ 1 mT, based on extrapolation of the resistively decaying field measured along the railgun nozzle;¹⁷ the ratio of magnetic field energy density to kinetic energy density is $\sim 10^{-4}$ and so we treat the interaction as unmagnetized. The intra-jet thermal collisionality is high, but the relevant collision length for determining the nature of the interaction at initial jet merging is the inter-jet ion collision length, which we show is long.

Diagnostics in the interaction region include a DiCam fast-framing (gate 20 ns) camera with a field of view reaching from one railgun nozzle to past chamber center (≈ 150 cm), a SpectraPro survey spectrometer with a view diameter of ≈ 1.5 cm near $z = 0$ cm, and an eight-chord laser interferometer^{23,24} with lines-of-sight spanning the interaction region at 7.5 cm intervals, from $z = -30$ cm to $z = 22.5$ cm (Fig. 2). The interferometer phase shift $\Delta\Phi$ is a line-integrated value sensitive to both free electrons and electrons bound in ions and neutrals; to determine n_i —here $\bar{Z} \geq 1$ and so $n_i \equiv n_e/\bar{Z}$ —requires knowledge of \bar{Z} and path length ℓ , which is es-

^{a)}Now at General Atomics, San Diego, CA; electronic mail: mosera@fusion.gat.com.

^{b)}Electronic mail: scotthsu@lanl.gov.

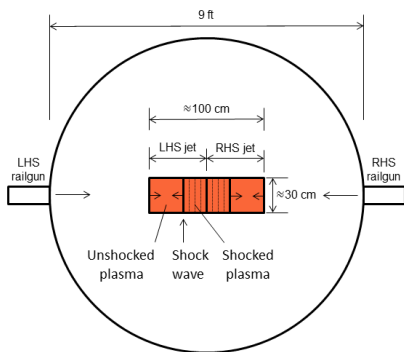


FIG. 1. Cartoon of experimental setup.

estimated from the full-width-half-maximum (FWHM) in a fast-camera image lineout at the spectrometer chord position divided by a factor of $\cos(30^\circ)$ to account for the angle between interferometer line-of-sight and jet axis. Spectrometer data and non-local-thermodynamic-equilibrium PrismSPECT^{25,26} calculations together give a lower bound on peak T_e and \bar{Z} based on the appearance or absence of spectral lines. Then n_i is calculated using $\Delta\Phi = C_e(\bar{Z} - Err) \int n_{tot} dl$, where $n_{tot} = n_n + n_i$ is the total ion-plus-neutral density ($\approx n_i$ in all cases here), $C_e = \lambda e^2 / 4\pi\epsilon_0 m_e c^2 = 1.58 \times 10^{-17} \text{ cm}^2$ is the phase sensitivity to electrons ($\lambda = 561 \text{ nm}$ is the laser wavelength), and $Err = 0.08$ represents an upper bound on the phase sensitivity to ions.¹⁷ PrismSPECT calculations are density dependent, and so the process is iterated until self-consistent n_i , T_e , and \bar{Z} are reached.^{16,19}

Fast-camera images (Fig. 2) give an overview of the two-jet interaction from diffuse emission at $t = 35 \mu\text{s}$ to a bright, well-defined structure at $t = 60 \mu\text{s}$. Interferometer measurements (Fig. 3; chords are into-the-page in Fig. 2) are from three sets of experiments: left-hand-side (LHS) jet only, averaged over 7 shots; right-hand-side (RHS) jet only, averaged over 7 shots; and merged-jet experiments, averaged over 14 shots. Shot-to-shot reproducibility is high;¹⁹ error bars indicating standard deviation are small except for late times when they are increased due to slight shifts in position of steep gradients. Comparing these data sets (Fig. 3) allows us to compare the merged-jet case with the superposition of the two individual jets expected for simple interpenetration.

Inter-jet collision lengths are calculated for ion-ion, ion-electron, and electron-electron collisions, taking all ion species into account; PrismSPECT calculations indicate that neutral density is $< 0.3\%$ at all times presented here and so we are justified in neglecting neutrals. Electron-electron collision length is $\ell^{e-e} = v_{th,e}/\nu_e$, using thermal collision frequency ν_e because the electron thermal velocity $v_{th,e} \gg v_{rel}$. We calculate both slowing and perpendicular collision length scales for ion-ion and ion-electron interactions, using $\ell = v_{rel}/\nu$ for all cases—except ion-ion slowing length scale $\ell_s^{i-i'} = v_{rel}/4\nu_s$ ²⁷—where the slowing frequency ν_s and perpendicular col-

TABLE I. Experimentally inferred plasma parameters and calculated collision lengths for the 40% argon mixture (90% argon mixture values, where different, are shown in parentheses). Collisionality estimates are qualitatively unchanged for the two mixture assumptions. Inclusion of 1% each carbon and hydrogen in both the 40% and 90% argon mixtures, and inclusion of 5% each carbon and hydrogen in the 40% argon mixture, leaves n , T_e , and \bar{Z} unchanged.

		$t=35 \mu\text{s}$	$t=40 \mu\text{s}$
n_i (10^{14} cm^{-3})		1.5 (1.9)	2.5 (2.4)
T_e (eV)		2.3 (1.7)	2.8
\bar{Z}		1.2 (1.0)	1.7 (1.8)
Z_i	Ar	1.2 (1.0)	1.8
	O	1.0	1.2
	Al	1.6 (1.1)	2.6
ℓ^{e-e} (cm)		0.054 (0.030)	0.035 (0.034)
ℓ_s^{i-e} (cm)	Ar	400 (360)	110
	O	220 (140)	92 (90)
	Al	160 (200)	37 (36)
$\ell_s^{i-i'}$ (cm)	Ar	1000 (2000)	140 (170)
	O	390 (500)	81 (92)
	Al	350 (950)	41 (48)
Interaction width (cm)		21–30	28–30

lision frequency ν_\perp are calculated in the slow limit for ion-electron and the fast limit for ion-ion.²⁸ In this parameter range $\ell_\perp > \ell_s$, and so we present only the latter. Electron-electron collision length is $\ell^{e-e} = v_{th,e}/\nu_e$, using thermal collision frequency ν_e because the electron thermal velocity $v_{th,e} \gg v_{rel}$. The total inter-jet ion-ion collision length for an ion species, taking interspecies collisions into account, is calculated by summing the collision frequencies for each collision type, e.g., for argon: $\ell_s^{\text{Ar}-i'} = v_{rel} / [4(\nu_s^{\text{Ar}-\text{Ar}} + \nu_s^{\text{Ar}-\text{O}} + \nu_s^{\text{Ar}-\text{Al}})]$.

In the case of ideal simple interpenetration, the interferometer trace in the two-jet experiment will be the sum of the two single-jet experiment traces. Figure 3 shows that the jet interaction is close to ideal simple interpenetration at early time, $t = 34\text{--}37 \mu\text{s}$: $\Delta\Phi$ in two-jet experiments is nearly identical to the sum of single-jet experiment $\Delta\Phi$ at all z positions for $t = 34\text{--}36 \mu\text{s}$ and within error bars for $t = 37 \mu\text{s}$ (Fig. 3). The merged-jet $\Delta\Phi = 3.1^\circ$ at $z = 0 \text{ cm}$, $t = 35 \mu\text{s}$ (Fig. 3). Using $\bar{Z} = 1.2$ inferred from spectroscopic measurements and PrismSPECT calculations, and $\ell = 20 \text{ cm}$, this $\Delta\Phi$ corresponds to $n_i = 1.5 \times 10^{14} \text{ cm}^{-3}$. Single-jet interferometer traces (Fig. 3) indicate that both jets contribute to the total merged $\Delta\Phi$, making this an upper bound on n_i of each of the individual interpenetrating plasma jets. We determine relative velocity of the two merging jets from the time-resolved single-jet interferometer traces:¹⁹ a linear fit to the arrival time of $\Delta\Phi_{peak}$ at each chord gives a velocity of 41 km/s ($R^2 = 0.89$) for the LHS jet and 49 km/s ($R^2 = 0.48$) for the RHS jet. This velocity rep-

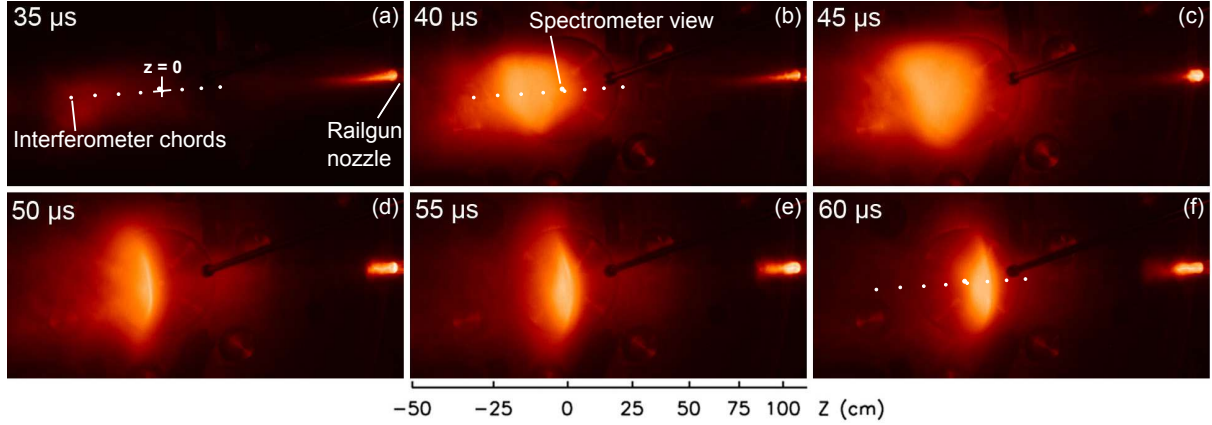


FIG. 2. False-color fast-camera images (shots #1834, 1833, 1836, 1837, 1838, 1845). Images are 12 bit and have been logarithmically scaled. Interferometer and spectrometer chord positions are indicated in (a), (b), and (f) for comparison with Figs. 3(b), (g), and (l), below. Lineouts in Figs. 5 and 6 are taken from approximately along the line of the interferometer chords indicated in (b) and (f), respectively.

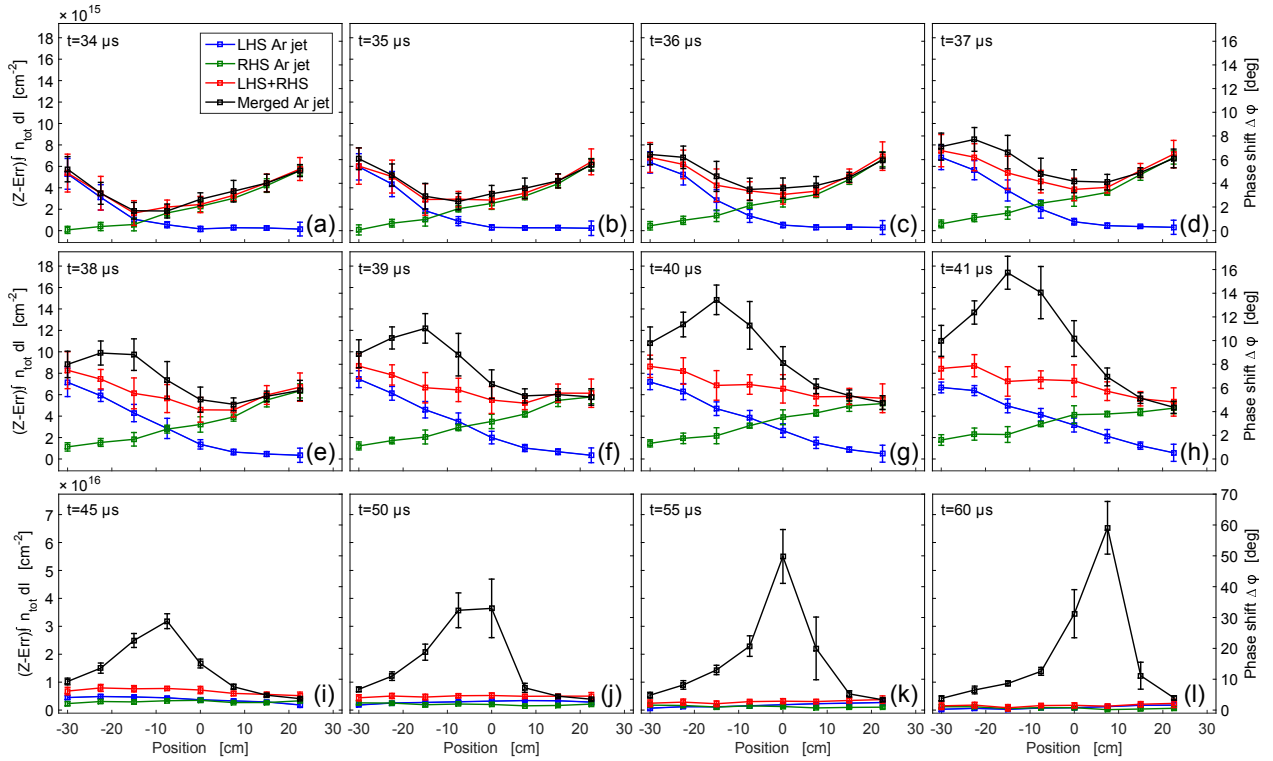


FIG. 3. Time-resolved interferometer measurements comparing single-jet (shots #1846-1860) and merged-jet (shots #1832-1845) experiments. Comparing average merged-jet traces (black) with the sum (red) of average single-jet traces (blue and green) shows that the jets interpenetrate for $t = 34\text{--}37\ \mu\text{s}$ (row 1), ionization increases the merged-jet phase shift for $t = 38\text{--}41\ \mu\text{s}$ (row 2), and the plasma has stagnated by $t = 60\ \mu\text{s}$ (row 3). Error bars indicate standard deviation. Note change in vertical scale and inter-plot time step between rows 2 and 3.

resents the jet bulk; the diffuse leading edge interacting here is moving at a higher velocity due to jet expansion, so the quoted velocities are a lower bound at $t = 35\ \mu\text{s}$, giving a conservative underestimate of collision lengths.

The appearance of emission at chamber center in two-

jet experiments, but not in single-jet experiments, suggests that the jets do interact, if minimally, as they interpenetrate at early time. This is confirmed by spectroscopic measurements at $z = 0\ \text{cm}$, $t = 35\ \mu\text{s}$, which give $T_e = 2.3\ \text{eV}$ [based on the appearance of the Ar II

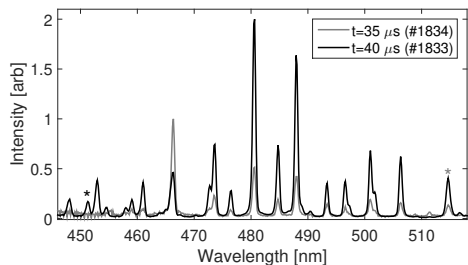


FIG. 4. Spectroscopic measurements for $t = 35 \mu\text{s}$ (shot #1834) and $t = 40 \mu\text{s}$ (shot #1833), near $z = 0 \text{ cm}$ [see Fig. 2(a) & (b) for spectrometer chord position]. Lines used to determine T_e , 514.7 nm (Ar II) for the $t = 35 \mu\text{s}$ case and 451.4 nm (Al III) for the $t = 40 \mu\text{s}$ case, are indicated with an asterisk.

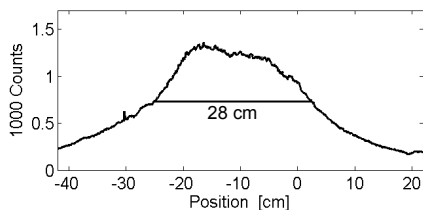


FIG. 5. Fast-camera image [Fig. 2(b)] lineout vs. z through $z = 0 \text{ cm}$ interferometer chord for $t = 40 \mu\text{s}$ (shot #1833). Horizontal line indicates FWHM=28 cm.

line at 514.7 nm, (Fig. 4)], greater than the $T_e = 1.9 \text{ eV}$ measured at the railgun nozzle. The experimentally inferred $\bar{Z} = 1.2$ is unchanged from nozzle to interaction region, so the only measurable interaction effect as the jets interpenetrate is a slight temperature increase.

The observation of jet interpenetration suggests that collisionality between ions of one jet and ions and electrons of the opposing jet is low. We verify this by calculating inter-jet collision lengths and comparing them to the scale size of the experiment. Using $v_{rel} = 90 \text{ km/s}$, $n_i = 1.5 \times 10^{14} \text{ cm}^{-3}$, $T_e = 2.3 \text{ eV}$, and $\bar{Z} = 1.2$, we calculate inter-jet collision lengths, presented in Table I. All ion collision lengths for $t = 35 \mu\text{s}$ are significantly longer than the length scale of the experiment, which we estimate as $\approx 21 \text{ cm}$ from a fast-camera image lineout or $\approx 30 \text{ cm}$ based on interferometer values. This is consistent with the observation that the jets interpenetrate.

As the higher-density bulk of the jet arrives at chamber center (leading edges are interpenetrating at $t = 35 \mu\text{s}$; $\Delta\Phi_{peak}$ reaches chamber center at $t \approx 42$ and $46 \mu\text{s}$ for the LHS and RHS jet, respectively), the collision scale lengths drop and \bar{Z} increases. At $t = 40 \mu\text{s}$ the two-jet $\Delta\Phi$ is greater than the sum of single-jet $\Delta\Phi$ in the region from $z = -22.5$ to -7.5 cm (Fig. 3).

An increase in merged-jet $\Delta\Phi$ over the sum of single-jet $\Delta\Phi$ indicates that the jets are no longer simply interpenetrating. The merged-jet phase shift at $z = 0 \text{ cm}$, $t = 40 \mu\text{s}$ is $\Delta\Phi = 8.1^\circ$, for which our iterative process (using $\ell = 22 \text{ cm}$) gives $n_i = 2.5 \times 10^{14} \text{ cm}^{-3}$,

$T_e = 2.8 \text{ eV}$ [based on the appearance of the Al III line at 451.4 nm, (Fig. 4)], and $\bar{Z} = 1.7$. Again, because the jets have interpenetrated, this bounds the n_i of the individual jets. Table I lists collision scale lengths calculated with these values. The increase in $\Delta\Phi$ in the merged-jet case over the simple-interpenetration case is consistent with a \bar{Z} increase rather than an n_i increase at $t = 40 \mu\text{s}$. The inferred $\bar{Z} = 1.7\text{--}1.8$ is a factor of $\approx 1.4\text{--}1.8$ greater than the $\bar{Z} = 1.0\text{--}1.2$ for interpenetrating jets at $t = 35 \mu\text{s}$.²⁹ The ratio of the $\Delta\Phi$ in the merged-jet case to $\Delta\Phi$ for the sum of single jets at $z = 0 \text{ cm}$, $t = 40 \mu\text{s}$ is $8.1^\circ/5.9^\circ \approx 1.4$; thus, increased ionization is sufficient to account for the increase in $\Delta\Phi$ between the two cases.

Interferometer measurements at $t = 40 \mu\text{s}$ indicate that the width of the $\Delta\Phi$ increase is 15–30 cm (the difference between merged-jet and single-jet $\Delta\Phi$ exceeds error bars at $z = -22.5, -15, -7.5 \text{ cm}$ but not at $z = -30, 0 \text{ cm}$). The region of increased emission in fast camera images aligns with the increased $\Delta\Phi$ in interferometer measurements [compare Figs. 2(b) and 3(g)]. A horizontal lineout of the fast-camera image shows that the region of increased emission has a FWHM of 28 cm (Fig. 5). Both of these estimates are of the same order as $\ell_s^{Al-i'} \approx \ell_s^{Al-e} \approx 40 \text{ cm}$ at $t = 40 \mu\text{s}$. Because the slowing lengths have now dropped to the order of the interaction width, we expect to see plasma stagnation as the interaction progresses.

Plasma stagnation leads to formation of a large, pronounced peak in the interferometer trace, with $\Delta\Phi_{peak} = 59.1^\circ$, by $t = 60 \mu\text{s}$. Because shot-to-shot variation in $\Delta\Phi$ increases at later times, the interferometer data for the individual shot shown in the fast-camera image in Fig. 2(f) (#1845) is plotted along with the 14-shot-averaged data in Fig. 6(a). For the individual trace, a pronounced peak spanning two interferometer chords drops off to 1/8–1/3 the peak value on either side ($\Delta\Phi = 43.6^\circ$ and 57.7° to $\Delta\Phi = 13.1^\circ$ and 7.0°). This peak aligns with the region of increased emission in Fig. 3(f); a lineout of the image [Fig. 6(b)] shows that the increased emission has a FWHM of 12 cm and is centered between the two high- $\Delta\Phi$ chord positions. The spectrometer view is near $z = 0 \text{ cm}$ at the peak edge and measures $\Delta\Phi = 43.6^\circ$; with $\ell = 29 \text{ cm}$ this corresponds to $n_i = 1.3 \times 10^{15} \text{ cm}^{-3}$, $T_e = 2.2 \text{ eV}$, and $\bar{Z} = 1.4$. A jet velocity of 45 km/s corresponds to Mach number $M \approx 8.5$ (calculated with $t = 40 \mu\text{s}$ plasma values), implying minimal expansion of the plasma normal to the jet velocity. Because $\ell = 29 \text{ cm}$ may be an underestimate, we also evaluate plasma conditions assuming $\ell = 44 \text{ cm}$ (estimated from the full-width-10%-maximum), obtaining $n_i = 6.6 \times 10^{14} \text{ cm}^{-3}$, $T_e = 2.4 \text{ eV}$, and $\bar{Z} = 1.5$.

The stagnated plasma has led to structure consistent with collisional shocks by $t = 60 \mu\text{s}$, as inferred from the observed n_i -transition scale of $\leq 7.5 \text{ cm}$ [Fig. 6(a)] being comparable to the predicted shock thickness, which is of order the post-shock thermal ion mean-free-path $\lambda_{mfp,i}$.³⁰ We use a one-dimensional shock model, which is justified based on our observations of minimal expan-

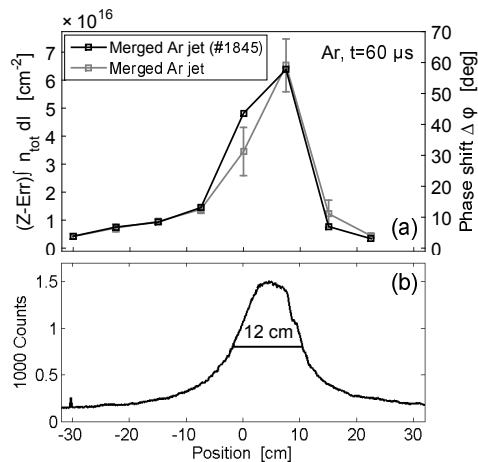


FIG. 6. (a) Interferometer measurements for $t = 60 \mu\text{s}$: merged-jet shot #1845 (black) and average of merged-jet shots (gray). Error bars indicate standard deviation. Structure is consistent with shock formation, with the peak in the black trace corresponding to postulated post-shock plasma, bounded on both sides by postulated shocks (the drop-off between chords at $z = 0$ and -7.5 cm and chords at $z = 7.5$ and 15 cm). (b) Fast-camera image lineout [Fig. 2(f)] vs. z through the $z = 0$ cm interferometer chord for $t = 60 \mu\text{s}$ (shot #1845). Increased emission aligns with peak, suggesting post-shock plasma in (a). Horizontal line indicates FWHM=12 cm.

sion normal to the jet velocity, to estimate post-shock ion temperature. Assuming that T_e does not change across the shock,³⁰ this predicts post-shock $T_i = 61$ eV for both cases calculated above, and shock width $\lambda_{mfp,i} \approx 2-3$ cm, consistent with the observed scale of ≤ 7.5 cm.

In summary, we have presented a concrete example of colliding supersonic plasmas in an initially collisionless regime for counter-streaming ions, transitioning from collisionless interpenetration to collisional stagnation owing to dynamically rising \bar{Z} . In the interpenetration stage, inter-jet collision lengths are much greater than the experimental length scale, consistent with simple interpenetration seen in interferometer measurements. In the increasing- \bar{Z} phase, the inter-jet ℓ_s^{i-e} and $\ell_s^{i-i'}$ are on the same order as the emission FWHM and width of the interferometer $\Delta\Phi$ peak. Finally, in the stagnation stage, $\ell_s^{i-i'}$ values decrease to the interaction region width, leading to structure consistent with collisional shock formation. These measurements provide an opportunity to validate fundamental physics models used to calculate plasma collisionality¹⁸ and ionization in plasmas with complex EOS.

ACKNOWLEDGMENTS

This work was supported by the LANL LDRD Program under DOE contract no. DE-AC52-06NA25396. We acknowledge J. P. Dunn and E. C. Merritt for technical support, and C. S. Adams and I. Golovkin for tech-

nical support and useful discussions.

- ¹S. Atzeni and J. Meyer-ter-Vehn, *The Physics of Inertial Fusion* (Oxford University, Oxford, 2004).
- ²R. Z. Sagdeev and C. F. Kennel, *Sci. Amer.* **264**, 106 (1991).
- ³H. Luna, K. D. Kavanagh, and J. T. Costello, *J. Appl. Phys.* **101**, 033302 (2007).
- ⁴O. Larroche, *Phys. Fluids B* **5**, 2816 (1993).
- ⁵P. W. Rambo and R. J. Procassini, *Phys. Plasmas* **2**, 3130 (1995).
- ⁶M. E. Jones, D. Winske, S. R. Goldman, R. A. Kopp, V. G. Rogatchev, S. A. Belkov, P. D. Gasparyan, G. V. Dolgoleva, N. V. Zhidkov, N. V. Ivanov, Y. K. Kochubej, G. F. Nasyrov, V. A. Pavlovskii, V. V. Smirnov, and Y. A. Romanov, *Phys. Plasmas* **3**, 1096 (1996).
- ⁷C. Thoma, D. R. Welch, and S. C. Hsu, *Phys. Plasmas* **20**, 082128 (2013).
- ⁸R. A. Bosch, R. L. Berger, B. H. Failor, N. D. Delamater, and G. Charatis, *Phys. Fluids B* **4**, 979 (1992).
- ⁹O. Rancu, P. Renaudin, C. Chenais-Popovics, H. Kawagashi, J. C. Gauthier, M. Dirksmoller, T. Missalla, I. Ushmann, E. Forster, O. Larroche, O. Peyrusse, O. Renner, E. Krouský, H. Pépin, and T. Shepard, *Phys. Rev. Lett.* **75**, 3854 (1995).
- ¹⁰A. S. Wan, T. W. Barbee Jr., R. Cauble, P. Celliers, L. B. DaSilva, J. C. Moreno, P. W. Rambo, G. F. Stone, J. E. Trebes, and F. Weber, *Phys. Rev. E* **55**, 6293 (1997).
- ¹¹J. S. Ross, S. H. Glenzer, P. Amendt, R. Berger, L. Divol, N. L. Kugland, O. L. Landen, C. Plechaty, B. Remington, D. Ryutov, W. Rozmus, D. H. Froula, G. Fiksel, C. Sorce, Y. Kuramitsu, T. Morita, Y. Sakawa, H. Takabe, R. P. Drake, M. Grosskopf, C. Kuranz, G. Gregori, J. Meinecke, C. D. Murphy, M. Koenig, A. Pelka, A. Ravasio, T. Vinci, E. Liang, R. Presura, A. Spitkovsky, F. Miniati, and H.-S. Park, *Phys. Plasmas* **19**, 056501 (2012).
- ¹²J. S. Ross, H.-S. Park, R. Berger, L. Divol, N. L. Kugland, W. Rozmus, D. Ryutov, and S. H. Glenzer, *Phys. Rev. Lett.* **110**, 145005 (2013).
- ¹³G. F. Swadling, S. V. Lebedev, G. N. Hall, F. Suzuki-Vidal, G. Burdiak, A. J. Harvey-Thompson, S. N. Bland, P. D. Grouchy, E. Khoory, L. Pickworth, J. Skidmore, and L. Suttle, *Phys. Plasmas* **20**, 062706 (2013).
- ¹⁴G. F. Swadling, S. V. Lebedev, A. J. Harvey-Thompson, W. Rozmus, G. C. Burdiak, L. Suttle, S. Patankar, R. A. Smith, M. Bennett, G. N. Hall, F. Suzuki-Vidal, and J. Yuan, *Phys. Rev. Lett.* **113**, 035003 (2014).
- ¹⁵K. F. Al-Shboul, S. S. Harilal, S. M. Hassan, A. Hassanein, J. T. Costello, T. Yabuuchi, K. A. Tanaka, and Y. Hirooka, *Phys. Plasmas* **21**, 013502 (2014).
- ¹⁶E. C. Merritt, A. L. Moser, S. C. Hsu, J. Loverich, and M. Gilmore, *Phys. Rev. Lett.* **111**, 085003 (2013).
- ¹⁷E. C. Merritt, A. L. Moser, S. C. Hsu, C. S. Adams, J. P. Dunn, A. M. Holgado, and M. A. Gilmore, *Phys. Plasmas* **21**, 055703 (2014).
- ¹⁸M. E. Jones, D. S. Lemons, R. J. Mason, V. A. Thomas, and D. Winske, *J. Comput. Phys.* **123**, 169 (1996).
- ¹⁹S. C. Hsu, E. C. Merritt, A. L. Moser, T. J. Awe, S. J. E. Brockington, J. S. Davis, C. S. Adams, A. Case, J. T. Cassibry, J. P. Dunn, M. A. Gilmore, A. G. Lynn, S. J. Messer, and F. D. Witherspoon, *Phys. Plasmas* **19**, 123514 (2012).
- ²⁰S. C. Hsu, T. J. Awe, S. Brockington, A. Case, J. T. Cassibry, G. Kagan, S. J. Messer, M. Stanic, D. R. Welch, and F. D. Witherspoon, *IEEE Trans. Plasma Sci.* **40**, 1287 (2012).
- ²¹S. C. Hsu, A. L. Moser, E. C. Merritt, C. S. Adams, J. P. Dunn, S. Brockington, A. Case, M. Gilmore, A. G. Lynn, S. J. Messer, and F. D. Witherspoon, *J. Plasma Physics* **FirstView**, 1 (2014).
- ²²F. D. Witherspoon, S. Brockington, A. Case, S. J. Messer, L. Wu, R. Elton, S. C. Hsu, J. T. Cassibry, and M. Gilmore, *Bull. Amer. Phys. Soc* **56**, 311 (2011).
- ²³E. C. Merritt, A. G. Lynn, M. A. Gilmore, and S. C. Hsu, *Rev. Sci. Instrum.* **83**, 033506 (2012).

- ²⁴E. C. Merritt, A. G. Lynn, M. A. Gilmore, C. Thoma, J. Loverich, and S. C. Hsu, *Rev. Sci. Instrum.* **83**, 10D523 (2012).
- ²⁵J. J. MacFarlane, I. E. Golovkin, P. R. Woodruff, D. R. Welch, B. V. Oliver, T. A. Mehlhorn, and R. B. Campbell, in *Inertial Fusion Sciences and Applications 2003*, edited by B. A. Hammel, D. D. Meyerhofer, and J. Meyer-ter-Vehn (American Nuclear Society, 2004) p. 457.
- ²⁶Prism Computational Sciences: www.prism-cs.com.
- ²⁷S. Messer, A. Case, L. Wu, S. Brockington, and F. D. Wither-
spoon, *Phys. Plasmas* **20**, 032306 (2013).
- ²⁸For ion-ion collisions, we use a correction to the Coulomb logarithm (see Appendix B of Ref. 17) for counterstreaming ions in the presence of warm electrons given in the NRL Plasma Formulary (2013 edition).
- ²⁹The observed rise in \bar{Z} on an $\approx 5\text{-}\mu\text{s}$ time scale cannot be readily explained by simple electron-impact (e.g., based on rate-coefficient data³¹) nor ion-impact³² ionization. Further work beyond the scope of this paper is needed to detail the probable ionization mechanisms.
- ³⁰M. Y. Jaffrin and R. F. Probstein, *Phys. Fluids* **7**, 1658 (1964).
- ³¹H.-K. Chung, M. H. Chen, W. L. Morgan, Y. Ralchenko, and R. W. Lee, *High Energy Density Phys.* **1**, 3 (2005).
- ³²J. B. Hasted, *Physics of Atomic Collisions* (American Elsevier, New York, 1972) p. 566.